PAPER

Check for updates

Expanding the zinc precursor toolbox: a comparative study of precursors for thermal ALD of ZnO thin films

Jorit Obenlüneschloß, [ID] [a] Rajesh Pathak,[b] Vepa Rozyyev, [ID] [b] Anil U. Mane, [ID] [b] Thomas Gemming, [ID] [c] Detlef Rogalla,[d] Jeffrey W. Elam [ID] *[b] and Anjana Devi [ID] *[a,c,e,f]

Atomic layer deposition (ALD) of zinc oxide (ZnO) has been widely researched using diethyl zinc (DEZ)-based methods. The significant importance of thin films of ZnO as transparent conductive oxides (TCO) in opto-electronic devices and photovoltaics warrants examining alternative Zn precursors for ZnO ALD as potential replacements for the pyrophoric DEZ. In this study, we investigated three alternative Zn precursors: $Zn(EEKI)_2$, $Zn(DMP)_2$, ZnEt(HMDS), in the process development for high-quality ZnO thin films and compared them to DEZ. The ALD processes were studied using *in situ* spectroscopic ellipsometry. The properties of the ALD ZnO films were characterized using *ex situ* X-ray photoelectron spectroscopy (XPS), Rutherford backscattering spectrometry and nuclear reaction analysis (RBS/NRA), X-ray diffraction (XRD), atomic force microscopy (AFM), transmission electron microscopy (TEM), and ultraviolet-visible (UV/Vis) spectrophotometry. These measurements confirmed the formation of pure, stoichiometric, and polycrystalline ZnO films using all four Zn precursors. Although the selected precursors are chemically diverse Zn compounds, they all yielded saturating ALD processes and high-quality ZnO thin films at 200 °C. This study highlights the potential benefits of alternative zinc precursors in designing ALD processes for ZnO thin films.

Introduction

Zinc oxide (ZnO), the second most common oxide in Earth's crust after iron oxides, has evolved from its original role as a white pigment to current applications in cutting-edge science and technology.[1] This evolution has occurred due to the numerous equally attractive, and valuable properties of this group II–VI semiconductor: high transparency for visible light,[2] photoluminescence,[3] direct wide band gap (3.37 eV), and n-type semiconducting behavior.[4] Furthermore, ZnO exhibits high electronic conductivity when doped accordingly,[5–7] its hexagonal wurtzite structure features piezoelectric effects,[8] and it possesses high mechanical and chemical stability.[1] This collection of properties has enabled the use of ZnO in areas

such as nano-mechanical devices,[6] as transparent conductive oxide (TCO) in optoelectronic devices,[2,9] as transparent electrodes,[10] chemiresistive gas sensors,[11,12] and protective cathode coatings in batteries,[13] to name a few important examples. One of the most common uses of ZnO is aluminum-doped ZnO (AZO) as a TCO, which opens up a wide range of applications on its own. The significantly increased n-type conductivity enables applications such as photovoltaic devices[14,15] and conductive membranes.[16] For more insights into the various aspects of zinc oxide, the reader is referred to a recent review by Sharma *et al.*[17]

ZnO can be synthesized using various techniques, including mechanochemical, sol–gel, vapor transport, thermal oxidation, solvothermal, and hydrothermal methods, as detailed elsewhere.[1,18,19] In this study, we focus on the preparation of ZnO *via* atomic layer deposition (ALD), as it offers several benefits, including exceptional uniformity, homogeneity, and step coverage, which are specific to and essential for certain applications. ALD uses cyclic, sequential self-limiting half-reactions of a precursor and a co-reactant with the surface to be coated.[20] The reader is referred to a recent comparison of ALD to other techniques by Sibanda *et al.*[21]

Since ALD is based on chemical surface reactions, it inherently relies on precursors, the choice of which determines the operating principle of any ALD process. While the process

[a]*Inorganic Materials Chemistry, Ruhr University Bochum, 44801 Bochum, Germany. E-mail: a.devi@ifw-dresden.de*
[b]*Applied Materials Division, Argonne National Laboratory, Chicago, Illinois 60637, USA. E-mail: jelam@anl.gov*
[c]*Leibniz Institute for Solid State and Materials Research, IFW Dresden, 01069 Dresden, Germany*
[d]*RUBION, Ruhr University Bochum, Universitätsstr. 150, 44801 Bochum, Germany*
[e]*Chair of Materials Chemistry, Dresden University of Technology, 01069 Dresden, Germany*
[f]*Fraunhofer Institute for Microelectronic Circuits and Systems, IMS, 47057 Duisburg, Germany*

parameters vary widely, they are primarily governed by the precursor used. Any compound serving as an ALD precursor must be sufficiently volatile and thermally stable. To allow the deposition of any desired material, it must possess the necessary self-limiting reactivity towards the substrate surface, the co-reactant employed, and the surface after the co-reactant pulse and the induced reactions.[22,23] In particular, the reactivity at the surface's active sites guides the film growth and influences the material's properties. Additional factors in precursor selection include cost, environmental safety, health concerns (*e.g.*, toxicity or pyrophoricity), and equipment compatibility (*e.g.*, corrosion by metal halides).

In ALD studies of ZnO, the primary precursor has been diethyl zinc (DEZ) due to its high vapor pressure and the strong reaction with water.[24] ZnO ALD using the DEZ-water process was first introduced in 1994, replacing the zinc acetate water process, one of the earliest reported ALD processes.[25,26] Although ZnO ALD using DEZ/H_2O is highly reliable and valuable for numerous applications, its widespread reliance may have hindered the development of competing or alternative processes, potentially omitting the discovery of valuable properties and film growth characteristics. Nonetheless, successful tuning of material properties has been demonstrated for DEZ through careful process design, such as co-dosing oxygen or using super-cycle processes with plasma treatment.[27,28]

Several Zn precursor candidates offer a wide range of deposition behaviors. Historically, zinc halides have been used for chemical vapor deposition.[29] The first report of ZnO ALD used zinc acetate before zinc alkyls became the dominant precursor compounds for zinc materials.[26,30] The primary goal of zinc precursor compounds is to achieve volatility and high reactivity while maintaining thermal stability. It is a challenge to rival the high reactivity of DEZ. Despite being the first ALD precursor used for zinc-based materials, the oxygen-coordinated acetate has been replaced because it requires harsh and toxic co-reactants such as H_2S or HF.[26,31] Fully oxygen-coordinated precursors for zinc have been scarce since then for this very reason. The strong zinc–oxygen bond requires more energy to break, making these compounds less suitable for ALD, as evidenced by the harsh deposition conditions required, *e.g.*, temperatures exceeding 300 °C for acetate. Nonetheless, β-diketonate ligated precursors, such as tetramethyl-heptanedionate (thd), have made a brief appearance in ALD of zinc materials, but they required the reactive co-reagent H_2S and were used only to produce ZnS films.[32] Meanwhile, the fully oxygen-bound compounds are successfully employed in chemical vapor deposition (CVD) processes.[33]

Recently, new precursor compounds have emerged, aiming to provide alternative reaction chemistries and adress potential safety concerns associated with DEZ's highly pyrophoric nature and the risk of corrosive halide-based byproducts. Here, a notable example introduced by Mai *et al.* is the intermolecularly stabilized compound, bis(3-(*N,N*-dimethylamino)propyl) zinc(II), Zn(DMP)$_2$, which still relies on the reactivity of a Zn to carbon bond but is more stable through the dative N–Zn bonds of the amine-containing sidechain.[34] This compound

has been proven to be a practical, nonpyrophoric alternative to DEZ, especially for spatial ALD processes, as shown by Johnston, and for atomic-layer additive manufacturing (ALAM), as shown by Stefanovic independently.[35,36] Mixed oxygen-nitrogen coordinated ketoiminate-type compounds explored by O'Donoghue *et al.*, such as the bis(*N*-(2′-ethoxy-ethyl)-2-penten-2-on-4-iminate)zinc(II), Zn(EEKI)$_2$, and the aminoalkoxide ligand class investigated by Han *et al.* have expanded the Zn ALD precursor library.[37,38]

This study aimed to survey a range of zinc precursors to investigate and evaluate their ALD growth processes. We chose Zn precursors that use water as a co-reactant and are expected to share a common deposition temperature range. The limitation of thermal water processes was selected to reduce the impact of the co-reactant, thereby limiting the reactivity observed to the zinc precursors. The final precursor selection is shown in Fig. 1, comprising the benchmark DEZ, its stabilized analogue, Zn(DMP)$_2$, the non-alkyl precursor with mixed O,N-coordination, Zn(EEKI)$_2$, and the heteroleptic silylamide alkyl compound, ethyl(di(trimethylsilyl)lamidio)zinc(II) ZnEt (HMDS). This selection will allow comparison of the influence of the direct coordination environment of the metal center, the steric bulk of the ligands, kinetic effects induced by differences in stability, and the β-silicon effect in the HMDS-bearing precursor.

DEZ has been featured in numerous reports on thermal ALD, and ALD-type growth has been claimed for the temperature range of 120 °C to 200 °C.[39]

The first, more elaborate precursor chosen for this study, Zn(DMP)$_2$, has been used in low-temperature plasma-enhanced ALD processes for fabricating gas barriers and sensors. Despite its lower volatility than DEZ it still exhibits a satisfyingly high vapor pressure (1 Torr of vapor pressure at a temperature of 76 °C), enabling a moderate ALD evaporation temperature of 55 °C.[34] ZnO growth was achieved at temperatures as low as 60 °C, with the ALD window reported to be between 140 °C and 160 °C. Zn(DMP)$_2$ has also been used in zincone molecular layer deposition and has been tested for thermal ALD with water using long precursor pulse times of 10 s at 60 °C.[40] This first exploration of thermal ALD has been complemented by thermal spatial ALD processes, which report growth with water at temperatures between 105 °C and 165 °C,[36] and also at 180 °C.[35] To expand on this previous work, Zn(DMP)$_2$ is included in this study.

For Zn(EEKI)$_2$, the second more elaborate precursor herein, a thermal ALD process with water has been reported to work reliably at temperatures above 200 °C.[37] It is the precursor with the lowest volatility out of the selection with its evaporation temperature approximately 100 °C higher than that of Zn (DMP)$_2$ as revealed by on thermogravimetry (TG).[34,37]

The last candidate, heteroleptic zinc alkyl silylamide ZnEt (HMDS), originates from the MOCVD literature, which compares different zinc compounds with mixed ligands for application as vapor-phase deposition precursors. ZnEt(HMDS), among others, has been easily synthesized and found to have a high vapor pressure of 37 Torr at room temperature,[41] even
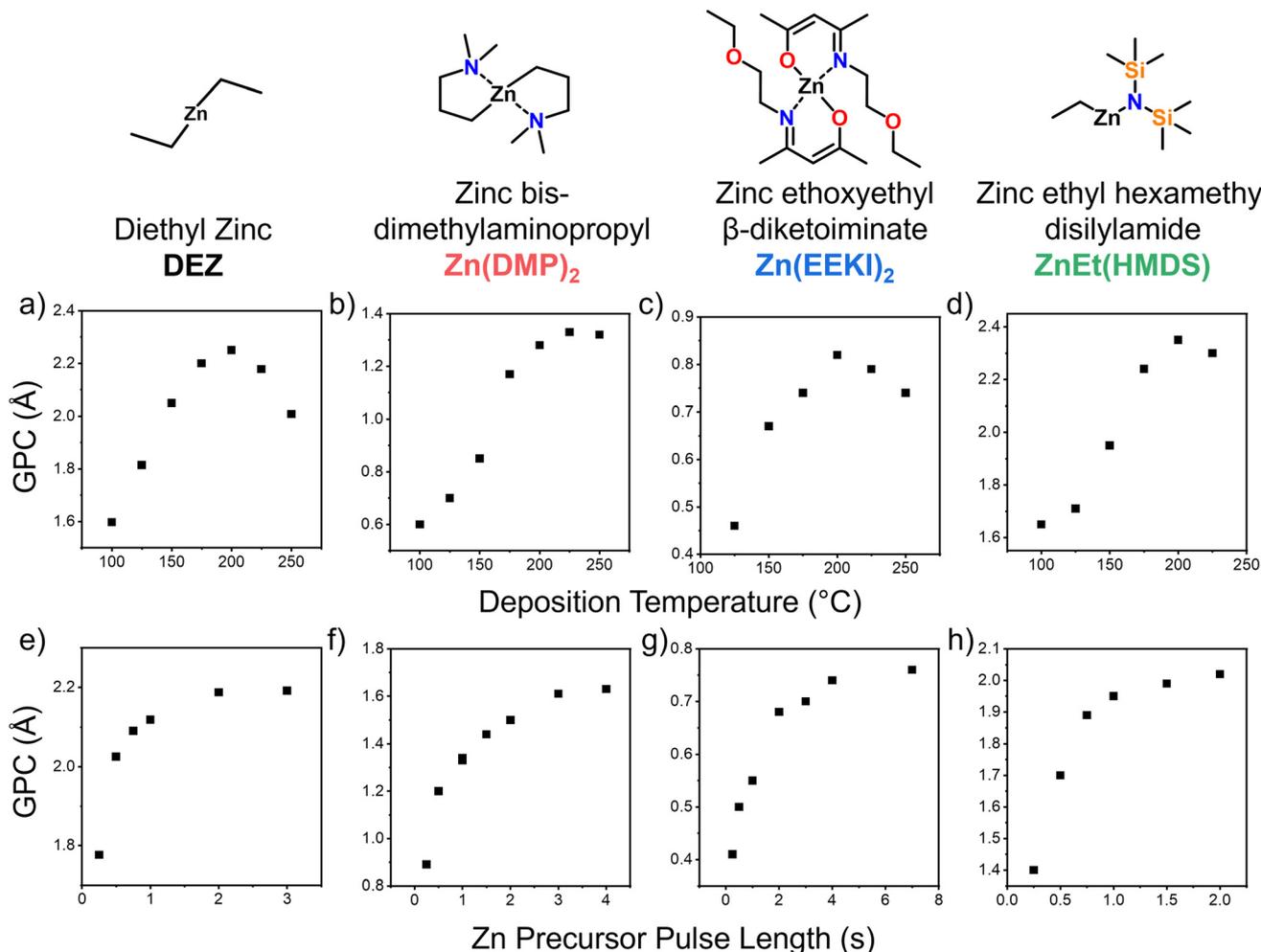
Fig. 1 ALD temperature and saturation behavior. Top: GPC *versus* deposition temperature. (a) DEZ pulse sequence 1–10–1–10, (b) Zn(DMP)$_2$ pulse sequence 1–10–1–10, (c) Zn(EEKI)$_2$ pulse sequence 2–10–2–10, (d) ZnEt(HMDS) pulse sequence 1–25–1–20. Bottom: GPC *versus* Zn precursor pulse length for the three Zn precursors at 200 °C. (e) DEZ pulse sequence x–10–1–10, (f) Zn(DMP)$_2$ pulse sequence x–10–1–10, (g) Zn(EEKI)$_2$ pulse sequence x–10–2–10, (h) ZnEt(HMDS) pulse sequence x–20–1–20. Please note the different axis scales.

surpassing DEZ (~22 Torr).[42,43] Despite this favorable property, to the best of our knowledge, it has not yet been utilized in any deposition process in the 25 years since its introduction.

DEZ, as the well-established precursor, benefits from proven production processes and facilities, making it likely the most cost-effective option. Among the other precursor candidates, ZnEt(HDMS) offers the simplest synthesis but depends on DEZ as a starting material. While Zn(DMP)$_2$ and Zn(EEKI)$_2$ are more synthetically complex, they demonstrate greater stability and can help avoid using the pyrophoric DEZ, thereby leading to significant safety cost savings.

With these four precursors available, we set out to investigate their thermal ALD behavior with water as a co-reactant. Initially, ALD behavior will be established for the four precursors, and the growth per cycle (GPC) will be determined as a function of the Zn precursor pulse length and the applied deposition temperature. In this study, the differences they induce in the deposited ZnO coatings will be assessed in

terms of purity, crystallinity, conductivity, morphology, and band gap. Furthermore, to gain a deeper understanding of the deposition mechanism, *in situ* spectroscopic ellipsometry (isSE) was performed to elucidate the growth process during the ALD half-reactions.

Results and discussion

ALD processes

Initially, the ALD process characteristics for the investigated precursors were assessed. To ensure comparability of the precursors, it is essential to define a working range for each one that overlaps as much as possible with the other precursors in the parameter space. Most importantly, the deposition temperature was studied to identify the "ALD window", or the temperature range where the GPC stays essentially constant. Once a suitable deposition temperature was determined for each pre-

Table 1 Optimized ALD process parameters for the zinc precursors investigated in this study. RT denotes room temperature

Zn precursor	Precursor T/°C	Co-reactant	Pulse purge sequence (precursor–purge–water–purge)/s	Growth per cycle/Å	Deposition T/°C
DEZ	RT	H_2O	2–10–1–10	2.2	200
$Zn(DMP)_2$	70		3–12–1–12	1.5	200
$Zn(EEKI)_2$	100		4–10–1–10	0.8	200
ZnEt(HMDS)	RT		1–15–1–15	2.3	200

cursor, the saturation with respect to precursor and co-reactant pulse lengths was investigated as described in the Experimental section. These growth parameters were analyzed using isSE and are summarized in Table 1 and Fig. 1. Measurements were performed on Si(100) wafers with native oxide after growing an initial ZnO surface with 25 DEZ/H_2O ALD cycles. This initial ZnO surface was used for all precursors to mitigate the potential nucleation effects of ZnO ALD on the Si(100) substrates. Temperature and pulse series were analyzed in two separate deposition runs.

DEZ

The established precursor DEZ has been used in over 150 processes and publications.[44] However, the DEZ/H_2O deposition process was adapted for the custom-built ALD system used for this study. Notably, the observed ALD growth window between 175 °C and 225 °C is higher than previously reported ones (Fig. 1a).[45,46] Saturation was achieved with DEZ pulses of 2 s or longer.

$Zn(DMP)_2$

In addition to the already reported PE-ALD process[34] and the spatial ALD processes,[35,36] a temporal thermal ALD process was fully developed for $Zn(DMP)_2$ in this work. It was expected that the water co-reactant would require higher deposition temperatures than the low-temperature oxygen plasma used earlier.[34] Moreover, the precursor delivery temperature had to be raised to 70 °C to ensure a satisfactory vapor pressure for the ALD equipment used. Unlike the plasma-enhanced ALD process previously reported, a GPC plateau was observed at higher deposition temperatures of 200 °C and above, rather than the increase in GPC previously seen at this temperature range.[34] For temperatures between 100 °C and 180 °C, a sharp rise in GPC was observed, unlike the plasma process, which showed a plateau in this temperature range. Similar to the ALD experiments performed by Stefanovic et al. at 150 °C, a GPC of 0.8 Å was observed.[36]

Clearly, $Zn(DMP)_2$ exhibits stability and follows an ALD-type growth mechanism at higher temperatures with water as a co-reactant. Here, the GPC plateaus at 1.3 Å; this value is slightly lower than the saturated GPC for the pulse length study (1.6 Å), as the study initially used shorter pulses (1 s). For the temperature study, the pulse length of 1 s was chosen based on the previously reported PE-ALD process, which required only 0.4 s, and the thermal process required only 8 ms to saturate in their respective ALD tool.[34,36] Stefanovic et al. reported

a similar behavior for $Zn(DMP)_2$ with respect to deposition and precursor delivery temperatures in their ALAM process.[36]

The saturation of the $Zn(DMP)_2$ precursor at 200 °C was demonstrated for pulses of 3 s and longer, which were subsequently used in depositions to achieve a GPC of 1.5 Å. It is reasonable to assume that increased absorption and desorption kinetics at this higher temperature necessitate longer exposures to saturate the surface. Supporting this, Stefanovic et al. found comparably long pulse times required to achieve saturation at 150 °C.[36]

$Zn(EEKI)_2$

For the mixed N,O-coordinated β-ketoiminate precursor $Zn(EEKI)_2$, O'Donoghue et al. reported full ALD process development using water as a co-reactant.[37] Thus, the aim was to replicate the known parameters and adapt them to the ALD tool as needed. With an adapted precursor evaporation temperature of 100 °C, the process conditions were investigated. The optimal growth temperature was confirmed at 200 °C, although the observed GPC was significantly lower, at 0.8 Å, compared to the previously reported 1.4 Å.[37] This discrepancy can be attributed to the differing reactor setup and the likely higher tool surface area for the tool used herein. For the temperature series, the ALD window could not be determined as precisely as before. The deposition performed at 200 °C corresponds to a maximum in GPC followed by a drop at the higher temperatures subsequently tested. For the optimal precursor pulse duration, a pulse time of 4 s was required instead of 2 s. The water pulse length matched the previous results of about 2 s (Fig. S2c). Overall, the adaptation of $Zn(EEKI)_2$ for thermal ALD was successful, largely consistent with the previously reported behavior.

ZnEt(HMDS)

The ZnEt(HMDS) precursor needed complete ALD process development, as no process data had been published before. Its high vapor pressure allows it to be vaporized at room temperature. Very high GPCs were observed across the temperature range of 100 °C to 225 °C, comparable to those of DEZ at temperatures above 200 °C. Saturation behavior was observed at temperatures above 175 °C, with GPC values reaching up to 2.3 Å, slightly exceeding those of DEZ. At 200 °C, saturation was achieved for precursor pulses longer than 1 s, whereas the water pulse saturated after 0.25 s (Fig. S2d). During the purge step after the ZnEt(HMDS) pulse, increased pressure hysteresis was observed in the reactor chamber, prompting an extension of the purge time to 15 s. Shorter purges were sufficient for

other precursors and did not affect the growth, even at reduced purge times.

It was possible to demonstrate the thermal ALD characteristics for DEZ and all other tested precursors, $Zn(DMP)_2$, $Zn(EEKI)_2$, and ZnEt(HMDS), using isSE measurements (Fig. 1). Saturation behavior could be established for the Zn precursor pulse lengths, and an "ALD window" plateau was observed with respect to deposition temperature. Further, the water pulse saturation for the four precursors is shown in Fig. S2. To ensure the best comparability across different processes for the following investigations, a single deposition temperature will be selected where all precursors perform well. This approach enables the attribution of differences in process outcomes and materials to the specific precursor chemistry used. Conveniently, all precursors share 200 °C as the growth temperature at which saturation occurs, aligning well with the ALD window. Additionally, maintaining a temperature of 200 °C is supported by reports of low defect density combined with good crystallinity, as indicated by the photoluminescence spectra of DEZ-water deposited films. The presence of OH groups at lower temperatures and decomposition at higher temperatures is believed to negatively impact film quality.[47] Moreover, previous spatial ALD studies using $Zn(DMP)_2$ also identified 200 °C as the optimal deposition temperature, taking composition and the ALD window into account.[36] Regarding pulse lengths, compounds with simple alkyl groups such as DEZ and ZnEt(HMDS) showed the earliest saturation, confirming the high reactivity of the zinc–carbon bonds in these compounds. In contrast, $Zn(DMP)_2$, which also features a Zn–C bond, required significantly longer pulses to achieve saturation. This is likely due to its lower vapor pressure, which may lead to a reduced precursor dose. The stabilizing effect of back-donating amine groups is also expected to influence the kinetics while preventing excessive exposure of the zinc center. $Zn(EEKI)_2$ required the longest pulses to reach saturation, due to its vapor pressure, dosing behavior, bulky bidentate ligands, and side chain. These factors can initially block surface sites but may rearrange over time, allowing more precursor molecules to adsorb. Furthermore, $Zn(EEKI)_2$ is presumed to be less reactive than the other precursors, due to its bidentate nitrogen and oxygen ligands, compared to precursors with at least one highly reactive Zn–C bond.

To investigate the effect of the different ligands, the ALD half-reactions were regarded in more detail by focusing on a single cycle in isSE (Fig. 2). Notable differences are apparent in the precursor adsorption, as evidenced by the increase in thickness from the fitted ellipsometry data, and in the reactivity with water of the adsorbed precursor species, as indicated by the decrease in thickness from the fitted ellipsometry data. DEZ, $Zn(DMP)_2$, and to a lesser extent $Zn(EEKI)_2$ and ZnEt(HMDS) show an equilibration of the surface species right after the precursor pulse, seen as a thickness decrease or desorption, during the purge step after the precursor pulse. This indicates that initial physisorption occurs alongside chemisorption for these precursors, with the physisorbed precursor molecules desorbing during the purge step. $Zn(EEKI)_2$ and
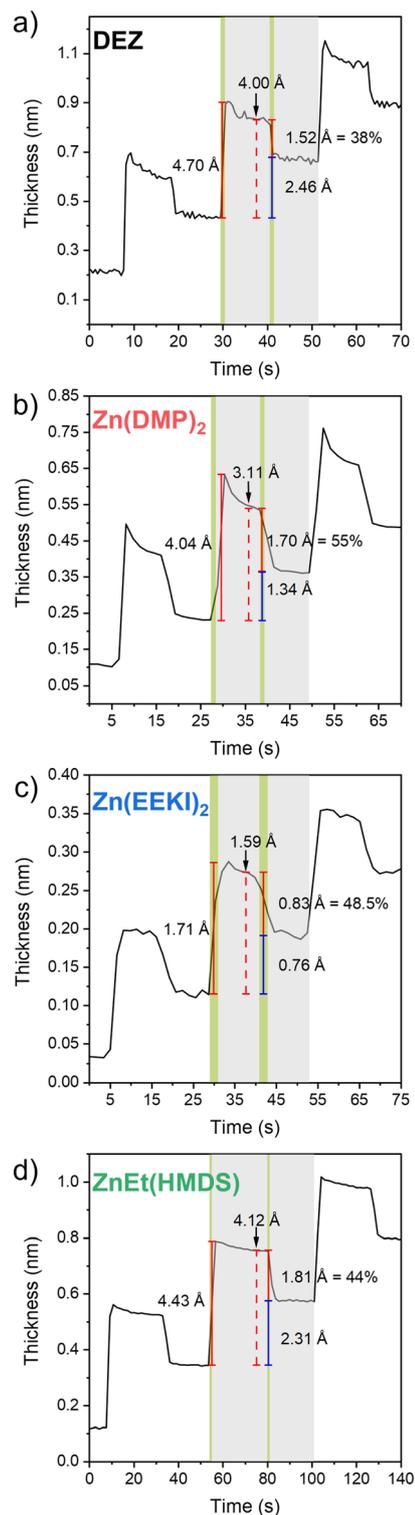

Fig. 2 *In situ* spectroscopic ellipsometry of growth cycles for each precursor at 200 °C; (a) DEZ, (b) $Zn(DMP)_2$, (c) $Zn(EEKI)_2$, (d) ZnEt(HMDS). Green areas indicate the precursor and water pulses, while greyed-out areas denote the purge times of the cycle in focus. Dashed red lines measure the equilibrated growth after precursor desorption during the purge step.

ZnEt(HMDS) exhibit this effect as well, but to a much lesser extent. For Zn(EEKI)$_2$, this can be attributed to its lower vapor pressure and lower dose during the precursor pulse, which does not achieve the same level of saturation in the gas phase, resulting in the large physisorption extent observed for DEZ and Zn(DMP)$_2$. However, ZnEt(HMDS) exhibits a high vapor pressure and shows a similar effect. Here, its surface reactivity is the more likely reason. For once, its surface reactivity is more defined: the ethyl ligand expected to be the more reactive functionality and react with the surface first, leaving the surface terminated with trimethylsilylamide. The trimethylsilyl termination is expected to exhibit a relatively nonpolar surface and be less susceptible to physisorption due to its reduced electrostatic interactions. This would result in a smaller amount of physiosorbed species, as evidenced by a smaller decrease in thickness during the purge step.

Another notable observation is the smaller increase in thickness observed for Zn(EEKI)$_2$ during the precursor pulse compared to the other precursors. This can be attributed to the lower reactivity of the O-, N-coordinating ligands *versus* the other precursors which feature at least one reactive alkyl ligand. Furthermore, the large size of the EEKI ligand, including its sidechain, can block the surface, resulting in lower surface coverage and a smaller increase in thickness.

Additionally, the reaction of the chemisorbed precursor species with water is investigated. The decrease in thickness upon the H$_2$O pulse can be regarded as a relative measure of ligand removal. The extent of the decrease can be linked to (1) the steric size of the ligands and (2) the surface coverage of the ligands. Here, especially DEZ attracts attention. It shows the lowest drop during the H$_2$O pulse of only 38% relative to the equilibrated thickness after the precursor pulse. The comparably lower decrease seen for DEZ can originate from the ethyl ligands, which are smaller than the ligands of the other precursors. Furthermore, this indicates the presence of the CVD component at elevated temperatures. When a degree of self-decomposition takes place during the precursor pulse already, the overall ligand removal during the water pulse is less pronounced. The most significant relative drop, 55%, is observed for Zn(DMP)$_2$. Here, the larger size of the DMP ligand and its higher surface coverage can be postulated. This would explain the lower GPC observed for Zn(DMP)$_2$ compared to DEZ, despite both precursors featuring highly reactive Zn–C bonds. Zn(EEKI)$_2$, which also features a large ligand, exhibits the second-largest relative drop, at 48.5%. Here, too, the large ligand size and its surface coverage are probable reasons. It is further expected that the bulky precursor, combined with the bulky ligands left on the surface during the precursor pulse, causes the much lower thickness increase during the precursor pulse and hence the overall lowest GPC. Interestingly, the fourth precursor, ZnEt(HMDS), shows the largest nominal drop of 1.81 Å, but only a moderate relative drop of 44%. The moderate relative decrease for ZnEt(HMDS) indicates a moderate size of the trimethylsilylamide group, which is expected to be the ligand covering the surface, as well as a moderate level of surface coverage of this ligand. The significant nominal decrease, however, indicates that this coverage does not prevent precursor nucleation rather it allows many active sites to be accessed by the precursor, resulting in trimethylsilylamide groups remaining on the surface. The high surface accessibility of the precursor contributes to the high GPC, and the large number of trimethylsilylamide groups results in a significant decrease in thickness after the H$_2$O pulse.

Material characterization and comparison

Material comparison

After demonstrating that ALD-type growth behavior for the four precursors, the deposited materials were investigated in more detail. We prepared ALD ZnO films on Si with thicknesses of 13 nm, 9 nm, 10 nm, and 9 nm for the DEZ, Zn(DMP)$_2$, Zn(EEKI)$_2$, and ZnEt(HDMS) precursors, respectively. Initially, the purity and composition of the resulting films were examined. Here, X-ray photoelectron spectroscopy (XPS) and Rutherford backscattering spectrometry, combined with nuclear reaction analysis (RBS/NRA), were employed to elucidate the surface and bulk species, respectively (Fig. 3). XPS analysis revealed a high degree of similarity among the obtained thin films. After charge correction to the adventitious C 1s component (BE = 284.8 eV), the core level spectra of the Zn 2p, O 1s, and Zn LMM Auger peak showed very close resemblance to one another (Fig. 3a and Fig. S9). For the Zn 2p 3/2, a peak position of 1021 ± 0.2 eV was observed, which is notably lower, by 0.7 eV, than literature-reported values for ZnO.[37,48] However, the observed values are consistent with those reported in other studies.[38,49] For the O 1s peak, the main component matched the reported value for ZnO of 529.9 eV, while the as-introduced spectra also showed additional oxygen species (Fig. S7b).[37,48] The shoulder at higher binding energy may contain components at approximately 531.5 eV and 531.8 eV that can be assigned to oxygen vacancies or hydroxide species and oxygenated carbon, respectively (see Fig. S3b–S6b for assignment and fits).[50–52] After sputtering, their intensity is vastly reduced (Fig. 3b *vs.* Fig. S7b), indicating that defective parts of the film and oxygenated impurities are mostly present at the surface of the films and originate from the exposure to the ambient. The Zn LMM Auger peak is located at 989.0 ± 0.2 eV, which, along with the peak shape and modified Auger parameter[53] (α = 2010.2 eV) (Table S1), strongly indicates that ZnO has been deposited. Both the peak positions and α are in agreement with reported values for ZnO,[54–56] and are clearly distinguished from Zn metal, where a sharper peak would be observed around 992 eV and α = 2013.8 eV.[57,58]

While considerable amounts of carbon are detected in the C 1s core level for the as-introduced surfaces, they are entirely removed after sputtering. Hence, the observed carbon can be attributed exclusively to adventitious species. Only for the ZnO film deposited from Zn(EEKI)$_2$, a small amount of carbon of 1.3 at% is detected in the film after sputtering. XPS detected
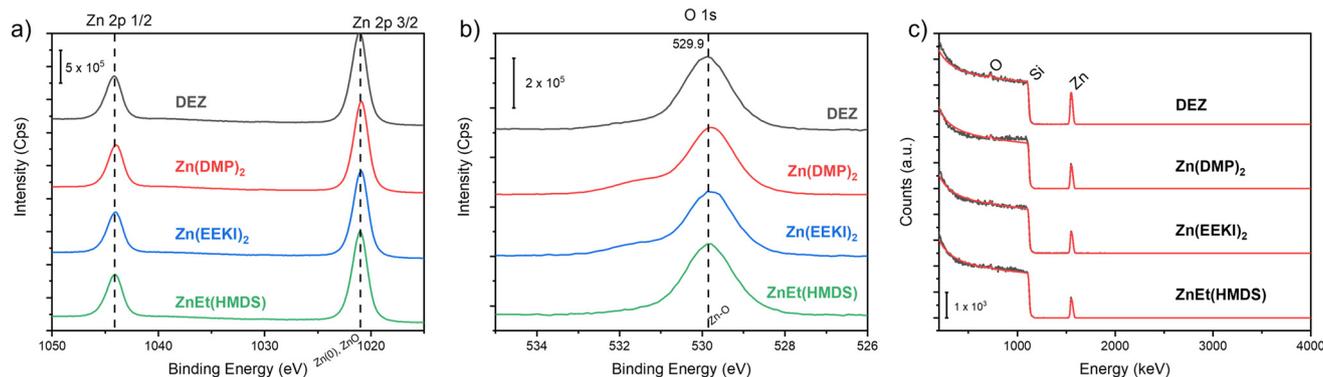
Fig. 3 XPS core level spectra of (a) Zn 2p and (b) O 1s for sputtered ZnO film surfaces. (c) RBS spectra of the ALD ZnO thin films. The ZnO films were deposited on Si using the four different investigated precursors.

no quantifiable nitrogen; the N1s core-level spectrum showed only background noise. The $Zn(EEKI)_2$ film, by contrast, showed a minuscule nitrogen signal on its as-introduced surface, which was removed after sputtering (Fig. S8). Peak fits for the Zn 2p, O 1s, and C 1s high-resolution XPS data for each precursor are presented in Fig. S3–S6 of the SI.

For all films, a significant increase in the zinc-to-oxygen ratio was observed by XPS after sputtering. The films become seemingly zinc-rich in the bulk of the film, as shown in Table 2 and the XPS depth profiles in Fig. S10. This observation led to the assumption that preferential sputtering occurs, thereby altering the stoichiometry.[59–61] It has been reported that oxygen species are more easily etched than the metal content of the films, and previous reports on ZnO thin films prepared by magnetron sputtering or CVD have described very similar effects.[62,63] To confirm this assumption, RBS/NRA was conducted to analyze the bulk composition of the ZnO thin films.

As shown in Fig. 3c, all the recorded RBS curves display zinc signals along with a broad silicon continuum originating from the underlying substrate, which indicates that the entire bulk of the film has been analyzed. Because the analyzed samples have varying film thicknesses, the peak heights differ among the curves, as they are directly proportional to the amount of deposited material. However, these differences do not affect the relative compositions. The silicon continuum obscures most of the oxygen signal, so the

amounts of oxygen and other light elements were determined using NRA.

Table 2 summarizes the composition determined by RBS/NRA and XPS of the ZnO films as a function of the different precursors used. Here, by employing RBS, a near-perfect 1 : 1 ratio for Zn : O was observed for all the precursors, with only minor impurities present in the films apart from the carbon, which is attributed to the surface by XPS. Like the XPS data, where the N 1s core level signals were essentially below the detection limit (except for $Zn(EEKI)_2$), NRA could not detect a significant amount of nitrogen in the films either. Only for the mixed O,N-coordinated β-diketoiminate precursor, $Zn(EEKI)_2$, some nitrogen was incorporated at 2.3 at%. This finding can be explained by the fact that it is one of the two precursors with a direct metal-to-nitrogen bond that might remain in the film if surface reactions and bond cleavage don't proceed to completion at a certain failure rate. However, XPS showed that nitrogen was present only at the surface. This difference can be attributed to the different probing depths of XPS and RBS/NRA. For instance, if very little nitrogen is sparsely distributed throughout the film, it may amount to a few percent, as observed by NRA, but remain below the detection limit of XPS for individual scans. The other precursor featuring such a metal–nitrogen bond is the ZnEt(HMDS). The very low nitrogen content of 0.2 at% confirms that the HMDS ligand, upon protonation from either surface hydroxyl sites or the water co-reactant, is a very stable leaving group. Residual HMDS ligand

Table 2 Film composition determined from RBS/NRA and XPS. The corresponding ratios of Zn to O in the films are listed for each measurement. ALD ZnO films were prepared at 200 °C. Concentrations are given in at%

Zn Precursor	RBS/NRA[a]					XPS surface[b]				XPS after sputtering[b]			
	Zn	O	C	N	Zn/O ratio	Zn	O	C	Zn/O ratio	Zn	O	C	Zn/O ratio
DEZ	50.0	49.6	0.5	0.0	1.01	51.4	43.7	4.9	1.17	56.7	42.0	0.0	1.35
$Zn(DMP)_2$	47.6	46.2	6.2	0.0	1.03	43.5	45.9	10.6	0.95	54.9	45.1	0.0	1.22
$Zn(EEKI)_2$	47.8	44.2	5.8	2.3	1.08	42.8	45.6	11.6	1.01	53.3	43.9	1.3	1.21
ZnEt(HMDS)	49.1	49.3	1.5	0.2	1.00	45.5	47.7	6.8	0.95	56.2	43.8	0.0	1.28

[a] In all cases, a possible error bar of ±1.5 at% needs to be assumed. [b] In all cases, a possible error bar ≤1.0 at% needs to be assumed.

would also leave silicon in the film, but neither RBS/NRA nor XPS detected any notable silicon incorporation when using this precursor for ZnO depositions. Approximately 6 at% carbon was found by NRA in ZnO films deposited using Zn(DMP)$_2$ and Zn(EEKI)$_2$. For the latter, this is within the range previously observed at this temperature range.[37] For Zn(DMP)$_2$, this thermal ALD process leaves behind more carbon compared to the previous plasma process at 200 °C.[34] However, the remaining carbon in all thin films is limited to the surface, as XPS did not detect any carbon after sputtering (Fig. S7 and S10). Note that the NRA values represent the average carbon content across the entire thin film. Furthermore, the RBS/NRA measurements were performed after a brief storage period during which the ZnO thin films were kept in ambient conditions; therefore, they likely accumulated more adventitious carbon. The XPS composition indicates that the as-prepared surfaces exhibit a similar trend, with the Zn(DMP)$_2$ and Zn(EEKI)$_2$ films containing approximately 11 at% carbon. It appears that the surfaces remaining after deposition with these two precursors are either more likely to adsorb adventitious species or the final cleavage of the ligand in the last deposition cycle is less efficient. This might suggest the need for an additional Zn precursor pulse to complete a full cycle and ensure clean ZnO deposition. Ultimately, using both XPS and RBS/NRA confirmed the purity of the ZnO thin films for all tested precursors.

Atomic force microscopy (AFM) was used to assess the roughness and topography of ALD ZnO films and to identify potential differences in precursor growth behavior. Four AFM images are shown in Fig. 4 for the different precursors used. A distinct difference is observed between the films grown by DEZ and Zn(DMP)$_2$ compared to those grown from Zn(EEKI)$_2$ and ZnEt(HMDS). The AFM micrographs of the DEZ and Zn(DMP)$_2$ films show the most uniform surfaces. On the other hand, the films deposited from Zn(EEKI)$_2$ and ZnEt(HMDS) exhibit a more grainy, less uniform texture. In the case of Zn(EEKI)$_2$, these rougher areas are homogeneously dispersed and exhibit a uniform size distribution. In contrast, ZnEt(HMDS) also exhibits more pronounced features, in addition to the smaller features that can be observed. Whereas the films deposited by the bis-alkyl precursors, DEZ and Zn(DMP)$_2$, exhibit the ALD typical somewhat grainy texture with appreciable low root mean square roughness (RMS) of 0.2 nm. This is consistent with the reported processes, as the PEALD process using Zn(DMP)$_2$ yielded an RMS value of 0.18 nm for a film approximately half the thickness of the one fabricated and investigated here.[34] When DEZ is used, various RMS values have been reported in the literature. They were observed in the range of 0.6 nm (ref. 64) or around 1 nm,[65] but also up to 2 nm for ALD films grown at 200 °C.[66] The AFM scans of Zn(EEKI)$_2$ and ZnEt(HMDS) deposited films show similar features, albeit with different characteristics. With Zn(EEKI)$_2$, the roughest film overall had an RMS value of 0.8 nm. This could be explained by the large size difference of the ligands between this precursor and the others, which may cause nucleation sites to be located farther apart due to the ethoxy side chain blocking surface area, as suggested by the isSE analysis above. DEZ and Zn(DMP)$_2$, with their smaller ligands on the other hand, can be expected to achieve a higher surface coverage and upon the precursor dose, resulting in denser nucleation and a more uniformly closed film. Subsequently, film growth would continue coarsely, centered on fewer, more widely spaced nucleation sites. The ZnEt(HMDS) deposited film exhibits the highest inhomogeneity, with some features
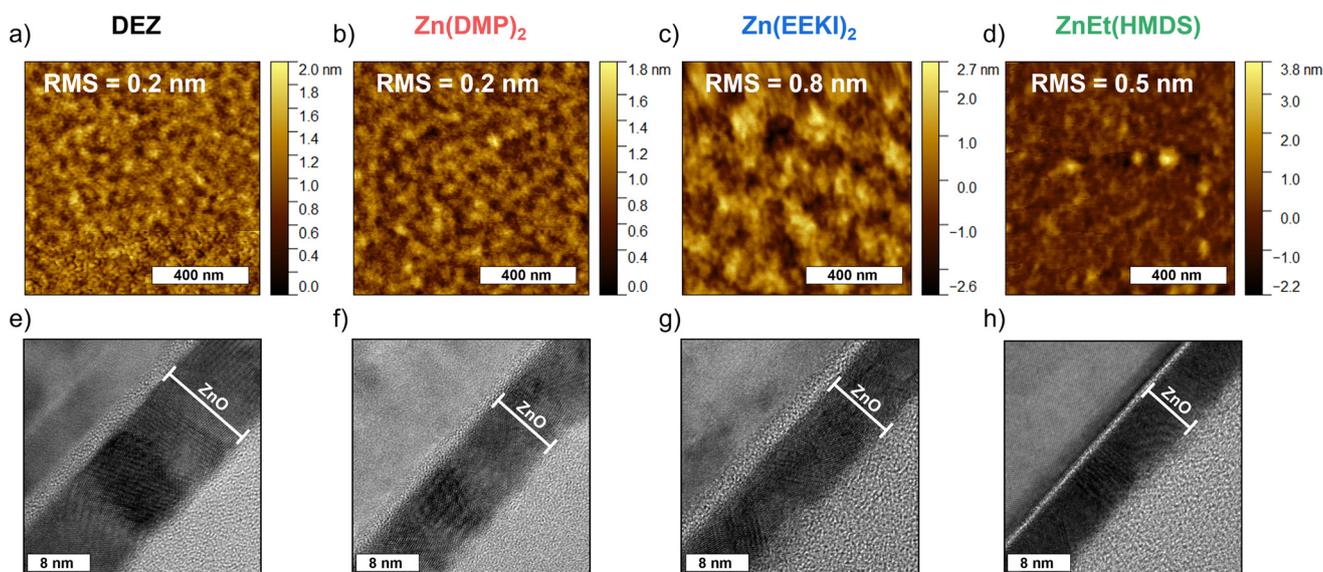

Fig. 4 AFM scans and TEM cross-section images of ZnO thin films deposited on Si at 200 °C by: (a and e) DEZ, with a film thickness of approx. 13–14 nm; (b and f) Zn(DMP)$_2$, with a film thickness of approx. 8.5–10.5 nm; (c and g) Zn(EEKI)$_2$, with a film thickness of approx. 10–11 nm; (d and h) ZnEt(HMDS), with a film thickness of approx. 8–9 nm.

protruding prominently from the surface, resulting in an increased RMS value of 0.5 nm. Whereas the surface excluding those features is more homogeneous, a similar RMS as for DEZ and Zn(DMP)$_2$ is expected in these areas.

A key metric for comparing different fabrication processes, particularly when considering precursors for the same material, is crystallinity. We investigated the crystallinity to elucidate potential differences in the nucleation and growth behavior of the four precursor compounds using transmission electron microscopy (TEM) (Fig. 4) and X-ray diffraction (XRD) (Fig. 5).

To initially assess the structure of the thin films, TEM measurements were performed on the different samples. In Fig. 4, cross sections of the four different samples are depicted. In the images, the top-left corner shows the crystalline Si substrate with approximately 2 nm of amorphous native SiO$_2$ on top, followed diagonally by the ZnO layer. The ZnO layer is then topped with a protective carbon layer visible in the bottom-right. All four films are polycrystalline with differently oriented crystalline domains that can be distinguished. Some amorphous regions can be seen between those crystalline domains. The thin films from all precursors are dense and uniform in thickness. Unlike the top-down AFM images, the four films appear very similar in their TEM cross-sections, and no significant protrusions were observed.

To further analyze crystallinity by XRD, thin-film samples with thicknesses of 30-40 nm were deposited at 200 °C and used exclusively for these measurements. The diffractograms shown in Fig. 5 indicate a similar degree of crystallinity within

Fig. 5 XRD diffractograms for ZnO thin films grown on Si(100) with the four different precursors. Displayed is the 2θ region with the most pronounced ZnO reflections, which are indexed. The grey area denotes reflections originating from the Si(100) substrate. The ZnO zincite phase reference pattern is taken from PDF no. 00-036-1451. The wavy pattern observed in the diffractograms of DEZ and ZnEt(HMDS) can be attributed to interference effects arising from the semi–crystalline nature of the films.

the obtained thin films, irrespective of the precursor used. Although the intensity of the 002 reflection is very similar, there are differences in the observed full width at half maximum (FWHM) values, as shown in Table S2. The narrowest reflection is observed for the films deposited from ZnEt (HMDS), indicating slightly larger crystallites. The broadest reflection is obtained with the film deposited from Zn(EEKI)$_2$, originating from the smaller crystallites. Possibly, the large EEKI ligand may block the surface, causing nucleation to occur at multiple initial nucleation sites instead of islands agglomerating in the early stage. For all films, the (002) orientation is the by far most pronounced, with only the ZnEt (HMDS) films showing an additional hint of the 101 reflection and only the Zn(EEKI)$_2$ showing the 113 reflection at 47.9°. In previously published work, Zn(EEKI)$_2$ deposited films exhibited the three 100, 002, and 101 reflections in GI-XRD.[37] The most pronounced reflection at 200 °C was the 101. Also, for higher temperatures, the 101 reflection remained the most intense reflection in that study. This change in preferred orientation is notable; only a partially satisfying explanation can be found in the different ALD reactors used in the previous and this study, with differing flow dynamics altering how the precursor reaches the surface. Seemingly, this is most pronounced for the Zn(EEKI)$_2$ with the largest ligand herein, where the orientation of the initial adsorption has a larger influence on the growing film. Furthermore, the ZnO film deposited using this precursor appears to have the most strained crystallites, with both the 002 and 113 reflections shifted by −0.35° and 0.23°, respectively. For DEZ, it has been shown that at higher temperatures, including 200 °C tested herein, the 002 orientation dominates.[67] The analysis of the crystallinity of the obtained films revealed only minor differences in terms of preferred orientation or degree of crystallinity. Despite differences in precursor chemistries and distinctly different growth mechanisms, the observed crystallinity is very similar, suggesting that the deposition temperature is the primary factor influencing ZnO thin-film crystallinity, as previously observed.[67,68]

The band gap can be influenced by composition, purity, and crystallinity. For semiconductors, the band gap is a key property, because it influences the carrier concentration, which affects the type and degree of a material's conductivity. These are important for ZnO, classified as a wide-band-gap semiconductor and its envisioned use cases, such as TCO in optoelectronic devices, or as a sensor.[69] The band gaps of the ZnO ALD films produced with the four different precursors are investigated using UV/Vis spectroscopy (Fig. S11) and estimated numerically *via* the Tauc relation.[70] Fig. 6 depicts the plotted graphs and the band gaps, which are determined as the points of intersection of the steepest adsorption tangent with the *y*-axis. For the investigated ALD films, the band gaps are notably lower than the reported bulk value of 3.37 eV or 3.30 eV.[4,71] Notably, the films obtained from Zn(DMP)$_2$ and ZnEt(HMDS) have an energy gap of approximately 3.20 eV, which is 0.17 eV lower than the reported bulk value. A decrease in the band gap has been linked to increased film crystallinity,
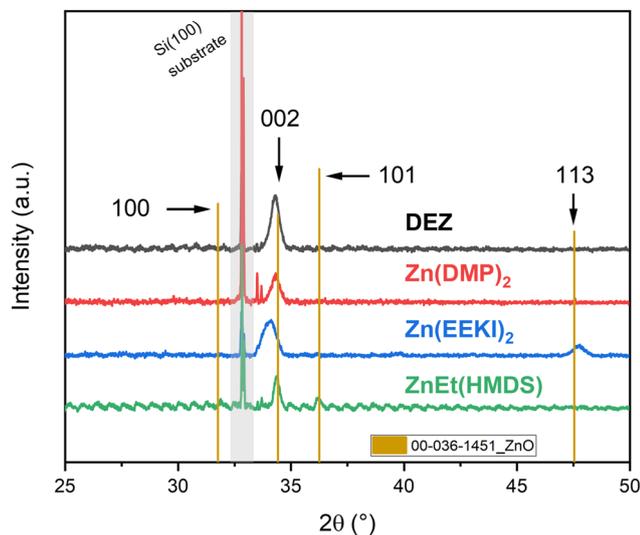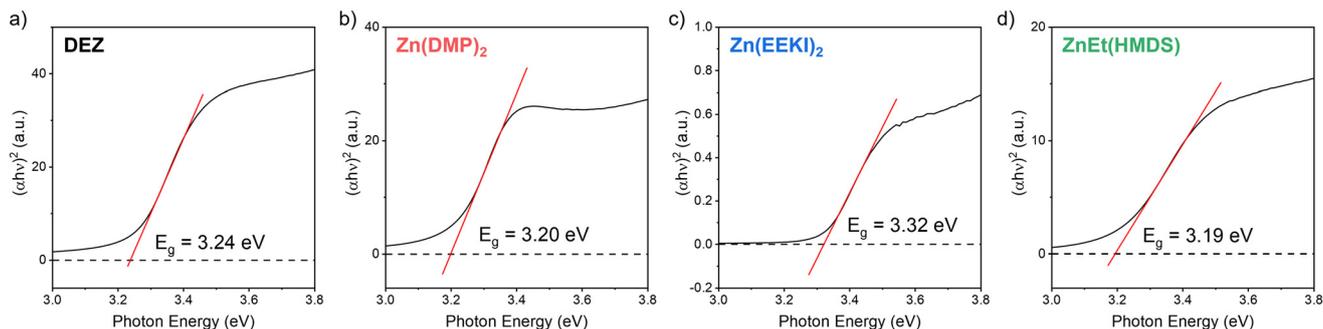
Fig. 6 Tauc plots from UV/Vis spectra of different ZnO ALD films from the selection of investigated precursors, (a) DEZ, (b) Zn(DMP)$_2$, (c) Zn(EEKI)$_2$, and (d) ZnEt(HDMS). The band gaps were calculated using the Tauc relation for direct transitions. Films were deposited onto quartz substrates.

as evidenced by a reduction in band gap reported with increasing annealing temperature.[72] A decreased band gap further suggests an increase in grain size; this is loosely reflected in the XRD patterns, which show similar crystallite sizes for DEZ and Zn(DMP)$_2$ with smaller crystallites and the largest band gap for Zn(EEKI)$_2$ and the largest crystallites and smallest band gap for ZnEt(HDMS), judging by the FWHMs of the 002 reflection.[49] The observed band gaps are lower than the bulk value, which can be attributed to a lower carrier concentration, possibly due to crystal imperfections and oxygen vacancies.[73]

Experimental

ALD process development

The growth of ZnO was performed in a hot-wall viscous-flow (https://www.sciencedirect.com/topics/physics-and-astronomy/viscous-flow) ALD reactor previously described, modified to accommodate an *in situ* ellipsometer, as described in the SI in more detail.[74,75] Ultrahigh-purity N$_2$ was used as a carrier gas with a total mass flow rate (https://www.sciencedirect.com/topics/chemistry/flow-kinetics) of 200 sccm and a background pressure of 0.9–1 Torr, as measured with a Baratron capacitance manometer. The reactor temperature was maintained using proportional–integral–differential controllers with an accuracy of ±0.03 °C. ZnO films were deposited through self-limiting binary ALD reactions of DEZ, Zn(DMP)$_2$, Zn(EEKI)$_2$, and ZnEt(HMDS) with HPLC-grade water. For each precursor, an optimized pulse scheme was adopted as described in Table 1. The DEZ, ZnEt(HMDS) sources and water were kept at room temperature (https://www.sciencedirect.com/topics/chemistry/ambient-reaction-temperature). Zn(DMP)$_2$ was heated to 70 °C, and Zn(EEKI)$_2$ was heated to 100 °C. ZnO ALD was carried out at temperatures ranging from 100 °C to 250 °C, depending on the precursor used.

Diethylzinc (95%) was obtained from Strem Chemicals, Inc. The HPLC-grade water was purchased from Sigma-Aldrich and used without further purification. The three investigated precursors Zn(DMP)$_2$, Zn(EEKI)$_2$, and ZnEt(HDMS) were synthesized and purified as described in the SI. All vapor-phase depositions were performed under inert conditions using ultrahigh-purity N$_2$ (UHP, 99.999%).

Thin film characterization

Film growth was monitored using an *in situ* spectroscopic ellipsometer (Film Sense FS-1), applying a modified Al$_2$O$_3$ Cauchy two-layer model, assuming a 2 nm layer of native SiO$_2$. Measurements were verified with an *ex situ* spectroscopic ellipsometer from J. A. Woollam model Alpha SE.

AFM measurements were carried out using a Bruker Dimension Icon in tapping mode at a frequency of 218 kHz, a line rate of 1 Hz, and a scan resolution of 512 × 512 pixels. The AFM images were then analyzed with the Gwyddion software suite to determine the R_{RMS} values of the ZnO film.[76]

TEM was performed on a Tecnai F30 (FEI) operated at 300 kV, equipped with a high-angle annular dark-field detector for scanning imaging and an energy-dispersive X-ray spectrometer (EDXS) (TEAM Octane T Optima EDS windowless, Edax/Ametek). Cross sections of the specimens were prepared using a dual-beam focused ion beam (FIB) microscope (Helios 5 CX, TFS) operated at 30 kV. As a final step in specimen preparation, a 5 kV ion beam was used to clean the samples, reducing damage from the FIB process. Cross-section images of the specimens were recorded using bright-field high-resolution TEM.

The XPS measurements were performed on a Thermo Fisher K-Alpha + spectrometer, and the spectra were analyzed using Thermo Fisher Avantage software. All the spectra were referenced to the C 1s peak at 284.8 eV. Sputtering was performed for 15 s per level at 2 keV over a 2 × 2 mm^2 raster. Shirley-type backgrounds were fitted for the quantification. The X-ray source was a microfocused monochromatic Al Kα (1487 eV) beam with a spot size of 400 μm. For the survey scans, a pass energy of 200.0 eV with a step size of 1.000 eV was used. For the high-resolution XPS measurements, 50.0 eV with a step size of 0.100 eV of pass energy was used. For charge compensation, a dual-beam electron flood gun (ultra-low energy coaxial electron and Ar$^+$ ion beam) was used. Depth profiling of the films was performed by Ar$^+$ ion sputtering. The XPS spectra were aligned with the adventitious C 1s peak posi-

tioned at 284.8 eV and analyzed using Thermo Fisher Avantage software.

XRD measurements were performed with a Bruker D8 Advance diffractometer θ–2θ geometry with CuKα (1.5418 Å) radiation in the 2θ range from 10° to 60°.

RBS analysis combined with NRA was used to determine the composition of the thin films at RUBION, the Central Unit for Ion Beams and Radionuclides at Ruhr University Bochum. For RBS measurements, a ^{4}He$^+$ beam with an energy of 2.0 MeV was directed at the sample at 7°. NRA measurements were performed with a ^{2}H$^+$ beam (1.0 MeV). The backscattered particles were detected at an angle of 160° using a Si detector with a resolution of 16 keV. The emitted protons were detected at an angle of 135° relative to the beam axis. The RBS/NRA data were analyzed employing the SIMNRA program.[77]

UV/Vis spectroscopy was performed using a double-beam spectrophotometer (Agilent Cary 5000) in transmittance mode for films grown on quartz substrates. The Tauc plots were calculated using the Tauc equation $(\alpha h\nu)^{\frac{1}{2}} = B(h\nu - E_g)$ for direct allowed transitions.[78]

Conclusions

In this work, we have demonstrated that all four investigated Zn precursors could deposit high-quality ZnO thin films. Using ZnEt(HMDS) as a precursor, we have developed a new thermal ALD process with an extraordinarily high GPC, rivaling that of DEZ. At a deposition temperature of 200 °C chosen for this study, all four precursors yielded ZnO thin films with water as a co-reactant, and their properties varied only within a narrow range. Even though three of the precursors, besides DEZ, contain heteroatoms, the thin films were of high purity, as confirmed by XPS depth profile measurements and stoichiometric as confirmed by RBS/NRA.

In terms of crystallinity and their band gap, all four materials fell within a narrow range of each other. The first analysis that revealed more significant differences was AFM: DEZ and Zn(DMP)$_2$, which behave very similarly, showing smooth surface morphologies, comparable roughness, and grainy textures. However, for Zn(EEKI)$_2$ and ZnEt(HMDS), more irregular surface morphologies were observed with higher roughness and some island-like features. To investigate these differences, we employed isSE and observed distinct growth modes of the precursors. While DEZ appears to undergo some self-decomposition, the other precursors leave more intact ligands attached to the surface. This is particularly evident for Zn(EEKI)$_2$, whose bulky ligands hinder growth and may lead to nucleation into islands as fewer nucleation sites can be populated during each cycle.

Through our work, we have highlighted that, in addition to the ubiquitous DEZ, alternative Zn precursors can be used to deposit ZnO of equal quality. Although the differences in the ZnO thin films grown in this work were insignificant, the choice of precursor can be vital when targeting ternary or quaternary material systems. There, the interplay among the different precursors, deposition temperatures, and co-reactants must be carefully considered. For these applications, it is valuable to have a broader library of Zn-precursors at hand, thereby enabling a more expansive parameter space.

Author contributions

J. Obenlüneschloß: ALD process development, material characterization, data interpretation, precursor synthesis, paper conception, and writing. Dr. R. Pathak: scientific support. Dr. V. Rozyyev: scientific support. Dr. T. Gemming: TEM measurements. Dr. A. Mane: supervision, experimental advice, paper conception, review, and editing. Dr. J. Elam: supervision, paper conception, review, and editing. Prof. Dr. A. Devi: supervision, paper conception, review, and editing.

Conflicts of interest

The authors declare no conflict of interest.

Data availability

The data supporting this article are included as part of the supplementary information (SI). Supplementary information is available. See DOI: https://doi.org/10.1039/d5dt02379c.

Acknowledgements

References

1 S. Raha and M. Ahmaruzzaman, *Nanoscale Adv.*, 2022, **4**, 1868–1925.

2 B. Tunhoo, S. Kaewkusonwiwat, T. Thiwawong and K. Onlaor, *J. Electron. Mater.*, 2022, **51**, 6903–6912.

3 J. Lim, K. Shin, H. Wookim and C. Lee, *J. Lumin.*, 2004, **109**, 181–185.

4 S. S. Shinde, P. S. Shinde, Y. W. Oh, D. Haranath, C. H. Bhosale and K. Y. Rajpure, *Appl. Surf. Sci.*, 2012, **258**, 9969–9976.

5 S. D. Ponja, S. Sathasivam, I. P. Parkin and C. J. Carmalt, *Sci. Rep.*, 2020, **10**, 638.

6 N. Van Toan, T. T. K. Tuoi, N. Inomata, M. Toda and T. Ono, *Sci. Rep.*, 2021, **11**, 1204.

7 L. Wen, B. B. Sahu, H. R. Kim and J. G. Han, *Appl. Surf. Sci.*, 2019, **473**, 649–656.

8 G. Wisz, I. Virt, P. Sagan, P. Potera and R. Yavorskyi, *Nanoscale Res. Lett.*, 2017, **12**, 253.

9 *Zinc Oxide Materials for Electronic and Optoelectronic Device Applications*, ed. C. W. Litton, D. C. Reynolds and T. C. Collins, John Wiley & Sons, Ltd, Weinheim, 1st edn, 2011.

10 Z. Chen, J. Wang, H. Wu, J. Yang, Y. Wang, J. Zhang, Q. Bao, M. Wang, Z. Ma, W. Tress and Z. Tang, *Nat. Commun.*, 2022, **13**, 4387.

11 M. A. Franco, P. P. Conti, R. S. Andre and D. S. Correa, *Sens. Actuator Rep.*, 2022, **4**, 100100.

12 K. G. Krishna, G. Umadevi, S. Parne and N. Pothukanuri, *J. Mater. Chem. C*, 2023, **11**, 3906–3925.

13 W. Chang, J.-W. Choi, J.-C. Im and J. K. Lee, *J. Power Sources*, 2010, **195**, 320–326.

14 H. Saarenpää, T. Niemi, A. Tukiainen, H. Lemmetyinen and N. Tkachenko, *Sol. Energy Mater. Sol. Cells*, 2010, **94**, 1379–1383.

15 G. Regmi, S. Rijal and S. Velumani, *Mem. – Mater. Devices Circuits Syst.*, 2023, **5**, 100064.

16 W. Yang, M. Son, R. Rossi, J. S. Vrouwenvelder and B. E. Logan, *ACS Appl. Mater. Interfaces*, 2020, **12**, 963–969.

17 D. K. Sharma, S. Shukla, K. K. Sharma and V. Kumar, *Mater. Today Proc.*, 2022, **49**, 3028–3035.

18 S. A. Colorado and H. A. Colorado, *Ceram. Int.*, 2017, **43**, 15846–15855.

19 M. Bakry, W. Ismail, M. Abdelfatah and A. El-Shaer, *Sci. Rep.*, 2024, **14**, 23788.

20 R. W. Johnson, A. Hultqvist and S. F. Bent, *Mater. Today*, 2014, **17**, 236–246.

21 D. Sibanda, S. T. Oyinbo and T.-C. Jen, *Nanotechnol. Rev.*, 2022, **11**, 1332–1363.

22 K. Bernal Ramos, M. J. Saly and Y. J. Chabal, *Coord. Chem. Rev.*, 2013, **257**, 3271–3281.

23 H. C. M. Knoops, S. E. Potts, A. A. Bol and W. M. M. Kessels, *Handbook of Crystal Growth*, Elsevier, 2015, pp. 1101–1134.

24 T. Weckman and K. Laasonen, *J. Phys. Chem. C*, 2018, **122**, 7685–7694.

25 V. Lujala, J. Skarp, M. Tammenmaa and T. Suntola, *Appl. Surf. Sci.*, 1994, **82–83**, 34–40.

26 M. Tammenmaa, T. Koskinen, L. Hiltunen, L. Niinistö and M. Leskelä, *Thin Solid Films*, 1985, **124**, 125–128.

27 R. Huang, S. Ye, K. Sun, K. S. Kiang and C. H. De Groot, *Nanoscale Res. Lett.*, 2017, **12**, 541.

28 D. Elam, E. Ortega, A. Nemashkalo, Y. Strzhemechny, A. Ayon, A. Ponce and A. A. Chabanov, *Appl. Phys. Lett.*, 2021, **119**, 142101.

29 T. Shiosaki, S. Ohnishi and A. Kawabata, *J. Appl. Phys.*, 1979, **50**, 3113–3117.

30 K. Kopalko, M. Godlewski, J. Z. Domagala, E. Lusakowska, R. Minikayev, W. Paszkowicz and A. Szczerbakow, *Chem. Mater.*, 2004, **16**, 1447–1450.

31 M. Ylilammi and T. Ranta-aho, *J. Electrochem. Soc.*, 1994, **141**, 1278–1284.

32 A. Short, L. Jewell, S. Doshay, C. Church, T. Keiber, F. Bridges, S. Carter and G. Alers, *J. Vac. Sci. Technol., A*, 2013, **31**, 01A138.

33 D. B. Potter, M. J. Powell, J. A. Darr, I. P. Parkin and C. J. Carmalt, *RSC Adv.*, 2017, **7**, 10806–10814.

34 L. Mai, F. Mitschker, C. Bock, A. Niesen, E. Ciftyurek, D. Rogalla, J. Mickler, M. Erig, Z. Li, P. Awakowicz, K. Schierbaum and A. Devi, *Small*, 2020, **16**, 1907506.

35 L. Johnston, J. Obenlüneschloß, M. F. Khan Niazi, M. Weber, C. Lausecker, C. S. Velasquez, L. Rapenne, H. Roussel, D. Bellet, A. Devi and D. Muñoz-Rojas, *RSC Appl. Interfaces*, 2024, **1**, 1371–1381.

36 S. Stefanovic, N. Gheshlaghi, D. Zanders, I. Kundrata, B. Zhao, M. K. S. Barr, M. Halik, A. Devi and J. Bachmann, *Small*, 2023, **19**, 2301774.

37 R. O'Donoghue, D. Peeters, D. Rogalla, H.-W. Becker, J. Rechmann, S. Henke, M. Winter and A. Devi, *Dalton Trans.*, 2016, **45**, 19012–19023.

38 S. H. Han, R. E. Agbenyeke, G. Y. Lee, B. K. Park, C. G. Kim, Y. K. Lee, S. U. Son and T.-M. Chung, *Dalton Trans.*, 2020, **49**, 4306–4314.

39 E. Guziewicz, M. Godlewski, L. Wachnicki, T. A. Krajewski, G. Luka, S. Gieraltowska, R. Jakiela, A. Stonert, W. Lisowski, M. Krawczyk, J. W. Sobczak and A. Jablonski, *Semicond. Sci. Technol.*, 2012, **27**, 074011.

40 A. Philip, L. Mai, R. Ghiyasi, A. Devi and M. Karppinen, *Dalton Trans.*, 2022, **51**, 14508–14516.

41 M. A. Malik and P. O'Brien, *Polyhedron*, 1997, **16**, 3593–3599.

42 M. Fulem, K. Růžička, V. Růžička, E. Hulicius, T. Šimeček, K. Melichar, J. Pangrác, S. A. Rushworth and L. M. Smith, *J. Cryst. Growth*, 2003, **248**, 99–107.

43 D. R. Stull, *Ind. Eng. Chem.*, 1947, **39**, 517–550.

44 Atomic Limits, 2025, DOI: 10.6100/ALDDATABASE.

45 A. Yamada, B. Sang and M. Konagai, *Appl. Surf. Sci.*, 1997, **112**, 216–222.

46 H. Makino, A. Miyake, T. Yamada, N. Yamamoto and T. Yamamoto, *Thin Solid Films*, 2009, **517**, 3138–3142.

47 D. Saha, A. K. Das, R. S. Ajimsha, P. Misra and L. M. Kukreja, *J. Appl. Phys.*, 2013, **114**, 043703.

48 L. V. Saraf, M. H. Engelhard, C. M. Wang, A. S. Lea, D. E. McCready, V. Shutthanandan, D. R. Baer and S. A. Chambers, *J. Mater. Res.*, 2007, **22**, 1230–1234.

49 R. Al-Gaashani, S. Radiman, A. R. Daud, N. Tabet and Y. Al-Douri, *Ceram. Int.*, 2013, **39**, 2283–2292.

50 Z. Li, H. Li, Y. Chen and M. Wang, *J. Mater. Sci.:Mater. Electron.*, 2024, **35**, 1359.

51 J. Duchoslav, R. Steinberger, M. Arndt and D. Stifter, *Corros. Sci.*, 2014, **82**, 356–361.

52 Z. Liu and F. Teng, *ChemistrySelect*, 2018, **3**, 8886–8894.

53 C. D. Wagner and A. Joshi, *J. Electron Spectrosc. Relat. Phenom.*, 1988, **47**, 283–313.

54 J. D. O. Primo, C. Bittencourt, S. Acosta, A. Sierra-Castillo, J.-F. Colomer, S. Jaerger, V. C. Teixeira and F. J. Anaissi, *Front. Chem.*, 2020, **8**, 571790.

55 M. S. Raven, *Surf. Interface Anal.*, 1979, **1**, 20–25.

56 C. Morales, A. Black, F. J. Urbanos, D. Granados, J. Méndez, A. Del Campo, F. Yubero and L. Soriano, *Adv. Mater. Interfaces*, 2019, **6**, 1801689.

57 L. S. Dake, D. R. Baer and J. M. Zachara, *Surf. Interface Anal.*, 1989, **14**, 71–75.

58 J. A. Rodriguez, T. Jirsak, J. Dvorak, S. Sambasivan and D. Fischer, *J. Phys. Chem. B*, 2000, **104**, 319–328.

59 C. Moore, J. Moon and D. Chidambaram, *Appl. Surf. Sci.*, 2024, **659**, 159876.

60 J. B. Malherbe, S. Hofmann and J. M. Sanz, *Appl. Surf. Sci.*, 1986, **27**, 355–365.

61 G. Greczynski and L. Hultman, *Appl. Surf. Sci.*, 2021, **542**, 148599.

62 S. Basu, P. K. Singh, C. Ghanshyam, P. Kapur and Y.-H. Wang, *J. Electron. Mater.*, 2012, **41**, 2362–2368.

63 S. Suh, L. A. Mîinea, D. M. Hoffman, Z. Zhang and W.-K. Chu, *J. Mater. Sci. Lett.*, 2001, **20**, 115–118.

64 C.-H. Zhai, R.-J. Zhang, X. Chen, Y.-X. Zheng, S.-Y. Wang, J. Liu, N. Dai and L.-Y. Chen, *Nanoscale Res. Lett.*, 2016, **11**, 407.

65 K.-J. Qian, S. Chen, B. Zhu, L. Chen, S.-J. Ding, H.-L. Lu, Q.-Q. Sun, D. W. Zhang and Z. Chen, *Appl. Surf. Sci.*, 2012, **258**, 4657–4666.

66 S. Mishra, E. Przezdziecka, W. Wozniak, A. Adhikari, R. Jakiela, W. Paszkowicz, A. Sulich, M. Ozga, K. Kopalko and E. Guziewicz, *Materials*, 2021, **14**, 4048.

67 E. Guziewicz, M. Godlewski, T. Krajewski, Ł. Wachnicki, A. Szczepanik, K. Kopalko, A. Wójcik-Głodowska, E. Przeździecka, W. Paszkowicz, E. Łusakowska, P. Kruszewski, N. Huby, G. Tallarida and S. Ferrari, *J. Appl. Phys.*, 2009, **105**, 122413.

68 G. Masmitjà, P. Estarlich, G. Lopez, I. Martín, C. Voz, M. Placidi, A. Torrens, E. Saucedo Silva, P. Vasquez, D. Muñoz, J. Puigdollers and P. Ortega, *J. Sci.:Adv. Mater. Devices*, 2024, **9**, 100698.

69 A. Adhikari, E. Przezdziecka, S. Mishra, P. Sybilski, J. Sajkowski and E. Guziewicz, *Phys. Status Solidi A*, 2021, **218**, 2000669.

70 P. Makuła, M. Pacia and W. Macyk, *J. Phys. Chem. Lett.*, 2018, **9**, 6814–6817.

71 V. Srikant and D. R. Clarke, *J. Appl. Phys.*, 1998, **83**, 5447–5451.

72 Mursal, Irhamni, Bukhari and Z. Jalil, *J. Phys.: Conf. Ser.*, 2018, **1116**, 032020.

73 C.-H. Hsu, X.-P. Geng, W.-Y. Wu, M.-J. Zhao, X.-Y. Zhang, P.-H. Huang and S.-Y. Lien, *Molecules*, 2020, **25**, 5043.

74 J. W. Elam, M. D. Groner and S. M. George, *Rev. Sci. Instrum.*, 2002, **73**, 2981–2987.

75 J. W. Elam and S. M. George, *Chem. Mater.*, 2003, **15**, 1020–1028.

76 D. Nečas and P. Klapetek, *Open Phys.*, 2012, **10**, 181–188.

77 M. Mayer, in *SIMNRA User's Guide*, Max-Planck-Institut für Plasmaphysik, Garching, 2020.

78 A. Escobedo-Morales, M. S. Pedraza-Chan, I. I. Ruiz-López, E. C. Anota, M. Salazar-Villanueva and D. Cortés-Arriagada, *Next Mater.*, 2026, **10**, 101412.